SIAM J. APPL. MATH.
Vol. 73, No. 3, pp. 1203–1223

A NEW PHYSIOLOGICAL BOUNDARY CONDITION FOR HEMODYNAMICS*

WILL COUSINS†, PIERRE A. GREMAUD†, AND DANIEL M. TARTAKOVSKY‡

Abstract. We propose a new physiologically-based outflow boundary condition for hemodynamics under general transient regimes. This is in contrast to previous studies that impose restrictions of temporal periodicity. The new condition is analyzed and its numerical implementation is discussed in detail. We show that existing impedance boundary conditions can be viewed as numerical approximations of the new condition. Our study provides a partial justification for using some of these existing conditions beyond the periodic problems for which they were designed. Moreover, the new condition has better stability properties. The theoretical results are illustrated by numerical experiments pertaining to cerebral blood flow.

Key words. hemodynamics, network, transport, modeling, boundary conditions, numerics

AMS subject classifications. 97M60, 65M70, 62P10, 76Z05

DOI. 10.1137/120895470

1. Introduction.

The complexity and size of human vasculature prevent the direct application of high fidelity mathematical models to the whole system. A common approach is to choose a small subset of arteries to model in detail, while accounting for the remainder of the vasculature through boundary conditions. This paper pertains to arterial—as opposed to venous—hemodynamics. Consequently, the inflow vessels, i.e., the inlets at the boundary of the computational domain, tend to be few in number and of significant size such as, for instance, the major cerebral arteries. By contrast, the outflow vessels, i.e., the outlets at the boundary of the computational domain, are smaller and more numerous. While it is feasible to impose, say, measured velocities on a few inflow vessels, it is impractical to do so on outflow vessels. In fact, discovering the behavior at the outlets is often the very aim of numerical hemodynamic studies [3, 24, 36].

We concentrate on outflow boundary conditions for one-dimensional formulations for two reasons. First, for several medical applications, a simple one-dimensional formulation may provide as much useful information as significantly more complex and computationally demanding full three-dimensional computations [13]. One-dimensional models have, for instance, been validated against data in [1, 5, 9, 10, 24, 27, 31]. Second, some boundary conditions for three-dimensional models can be derived and implemented from lower dimensional formulations [36]. In other words, the type of boundary conditions derived here may be useful for higher-dimensional models as well.

Several popular outflow boundary conditions for hemodynamics are based on an

*Received by the editors October 17, 2012; accepted for publication (in revised form) March 18, 2013; published electronically June 13, 2013.
http://www.siam.org/journals/siap/73-3/89547.html

†Department of Mathematics, North Carolina State University, Raleigh, NC 27695-8205 (wcousin@ncsu.edu, gremaud@ncsu.edu). The first author's work was partially supported by the National Science Foundation (NSF) through grant DMS-0636590 and East Asia and Pacific Summer Institutes (EAPSI) award 1015642. The second author's work was partially supported by the National Science Foundation (NSF) through grants DMS-0636590 and DMS-0811150.

‡Department of Mechanical and Aerospace Engineering, University of California, San Diego, La Jolla, CA 92093 (dmt@ucsd.edu). This author's work was partially supported by the Advanced Scientific Computing Research Program of the U.S. Department of Energy Office of Science.

electrical circuit analogy where blood pressure is thought of as voltage and flowrate as current. Such conditions include the pure resistor condition [29, 35], the three-element Windkessel model [2, 3, 10, 26, 28], and their variations. While these methods have been successfully used and do not require any periodicity assumptions, they are not physiologically based. Additionally, they are sensitive to internal resistances and capacitances that cannot be directly measured. These parameters have to be fitted for each specific patient to generate accurate model output [10, 14, 15, 16, 17].

Impedance boundary conditions are another type of outflow boundary condition for hemodynamics. The idea consists of evaluating, for each outflow vessel, the impedance corresponding to the presence of an entire vascular tree downstream from the edge of the computational domain. This procedure [22, 23, 24] relies on simplifying assumptions about both the nature of the flow (section 2.1) and the geometrical and topological structures of the tree (section 2.2). It combines an algorithm to compute the impedance of a vascular network [33] with linear wave theory [37, 38]. This approach is used, for instance, in [6, 8, 18, 30, 32, 34]. In [9], we derived an impedance boundary condition that is much simpler than, but similar to, Olufsen's [22, 23, 24]. All of these various incarnations of impedance boundary conditions have the advantage of being—at least to some extent—physiologically based. Their major shortcoming stems from the assumption of strict flow periodicity, which does not hold in many physiologically relevant conditions.

In this paper, we construct an impedance boundary condition that is valid for general transient flows. The main idea is to replace the Fourier series-based approach of [9, 22, 23, 24] by Laplace transforms (section 2). The method is implemented numerically in section 3 through a convolution quadrature approach [19, 20]. We discuss numerical experiments in section 5. We show that Laplace and Fourier series-based impedance conditions are similar since the Fourier series-based case is roughly an approximation of the more general Laplace case. The results from section 5 are supported by mathematical analysis results in section 4 and in the appendices.

2. Derivation of the method.

2.1. Single vessel equations. Consider flow in an elastic axisymmetric cylindrical vessel of radius R and length L. The incompressible Navier–Stokes equations are taken to be valid and are expressed in cylindrical coordinates. The flow itself is assumed to inherit the axial symmetry of the vessel and to present no "swirl," i.e., the angular component of the velocity is zero. Effects due to gravity are neglected. The position along the longitudinal axis is x and $\tilde{r}$ measures the distance from that axis. We take the following Ansatz for the longitudinal velocity:

$$u_x(\tilde{r}, x, t) = \frac{\gamma + 2}{\gamma} U(x, t) \left[1 - \left(\frac{\tilde{r}}{R(x, t)} \right)^{\gamma} \right], \tag{2.1}$$

where U is the cross-sectional average of the longitudinal velocity, and the fitting parameter $\gamma > 0$ is to be estimated. Note that $\gamma = 2$ corresponds to the classical Poiseuille flow.

The resulting equations are then averaged on cross-sections, leading to the one-dimensional formulation [7, 9, 10, 11, 28]

$$\partial_t A + \partial_x Q = 0, \tag{2.2}$$

$$\partial_t Q + \frac{\gamma + 2}{\gamma + 1} \partial_x \left(\frac{Q^2}{A} \right) + \frac{A}{\rho} \partial_x P = -2\pi(\gamma + 2) \frac{\mu}{\rho} \frac{Q}{A}, \tag{2.3}$$

where $A = \pi R^2$ is the cross-sectional area, $Q = AU$ is the flowrate, and μ and ρ are the (constant) viscosity and density of blood, respectively. The system is closed by assuming the wall to be thin and linearly elastic with a Poisson ratio of $1/2$ [4]. The resulting constitutive law for the pressure P is

$$P - P_0 = \frac{4Eh}{3r_0}\left(1 - \sqrt{\frac{A_0}{A}}\right), \tag{2.4}$$

where $A_0 = \pi r_0^2$ is a characteristic value of the cross sectional area of the unstressed vessel and E and h are the Young modulus and thickness of the vessel wall, respectively [23]. Finally, assuming small amplitude fluctuations, the system (2.2)–(2.4) is linearized in A around A_0, resulting in

$$C\,\partial_t P + \partial_x Q = 0, \tag{2.5}$$

$$\partial_t Q + \frac{A_0}{\rho}\,\partial_x P = -2\pi(\gamma+2)\,\frac{\mu}{\rho}\,\frac{Q}{A_0}, \tag{2.6}$$

where $C = dA/dP$ is the vessel compliance.

Instead of expressing the above unknowns in terms of their Fourier coefficients, as done in [9, 22, 23, 24, 32] among others, we take the Laplace transform of the system with respect to time. Assuming zero initial pressure and flow, we get

$$Cs\,\hat{P} + \partial_x \hat{Q} = 0, \tag{2.7}$$

$$(s+\delta)\hat{Q} + \frac{A_0}{\rho}\,\partial_x \hat{P} = 0, \tag{2.8}$$

where s is a generic complex number, $\hat{P} = \mathcal{L}(P)$, $\hat{Q} = \mathcal{L}(Q)$, and $\delta = 2\mu(\gamma+2)/(\rho r_0^2)$. The solutions to (2.7) and (2.8) evaluated at $x = 0$ are

$$\hat{Q}(0,s) = sd_sC\hat{P}(s,L)\sinh\left(\frac{L}{d_s}\right) + \hat{Q}(s,L)\cosh\left(\frac{L}{d_s}\right),$$

$$\hat{P}(0,s) = \hat{P}(s,L)\cosh\left(\frac{L}{d_s}\right) + \frac{1}{sd_sC}\hat{Q}(s,L)\sinh\left(\frac{L}{d_s}\right),$$

with $d_s^2 = A_0/[C\rho s(s+\delta)]$. Defining the impedance through its Laplace transform

$$\hat{Z}(x,s) = \frac{\hat{P}(x,s)}{\hat{Q}(x,s)} \tag{2.9}$$

yields

$$\hat{Z}(0,s) = \frac{\hat{Z}(L,s) + \frac{1}{sd_sC}\tanh L/d_s}{sd_sC\,\hat{Z}(L,s)\tanh L/d_s + 1}. \tag{2.10}$$

The above formula links the impedance at the beginning of the vessel to the impedance at its end. For s restricted to the imaginary axis, i.e., $s = i\omega$, $\omega \in \mathbb{R}$, (2.10) corresponds to the impedance found in [9] (see relation (13)) where Fourier series were used.

2.2. Generalization to structured vascular trees. Vascular trees are assumed to share the following structure:

1. Vessels end by bifurcating into two daughter vessels; vessels with radii smaller than a minimal value $r_{min} > 0$ terminate, i.e., they do not bifurcate.
2. There are two parameters α and β where $0 < \beta < \alpha < 1$ and for any parent/daughter vessels
$$r_{d1} = \alpha r_{pa} \quad \text{and} \quad r_{d2} = \beta r_{pa},$$
where r_{pa}, r_{d1}, and r_{d2} are the radii of the parent/daughter vessels, respectively.
3. There is a positive parameter λ such that for any vessel in the tree
$$\lambda = r/L.$$

These assumptions are classical in the field; see, for instance, [23]. The existence of the scaling factors ensures that the number of different size vessels grows only quadratically with the number of generations, instead of exponentially as would be the case for a general tree [9]. The scaling parameters α, β, and λ can be determined from data; see Table 5.3 and [23, 24]. The choice of r_{min} is more delicate [9] and is the object of current work. Validation studies of the classical "periodic" impedance condition can be in found in [9, 24, 31].

We follow [9, 22, 23, 24, 32] to compute the impedance of the entire tree by noting that (2.9), together with continuity of pressure and conservation of mass at each junction, leads to

$$\frac{1}{\hat{Z}_{pa}(L,s)} = \frac{1}{\hat{Z}_{d1}(0,s)} + \frac{1}{\hat{Z}_{d2}(0,s)} \text{ for any } s. \tag{2.11}$$

The impedances at the ends ($x = L$) of all terminal vessels are assumed to share a common constant value $\hat{Z}_{term}$, which is usually set to $\hat{Z}_{term} = 0$ [9, 23, 24]. For any s, a value for the impedance of the root vessel is obtained by recursively applying relations (2.10) and (2.11).

2.3. Algorithm to compute the impedance. Sections 2.1 and 2.2 describe how to compute $\hat{Z}(s)$ for a structured tree. We give a recursive algorithm for performing this task. In the following, the function "singleVesselImp" denotes (2.10).

procedure IMPEDANCE
Input: r – radius of vessel
Output: ZPA_0
  if $r < r_{min}$ **then**
    $ZPA\_L = Z_{term}$
  else
    $ZD1 =$ IMPEDANCE$(\alpha \cdot r)$,
    $ZD2 =$ IMPEDANCE$(\beta \cdot r)$,
    $ZPA\_L = ZD1 \cdot ZD2/(ZD1 + ZD2)$,
  end if
  $ZPA\_0 = singleVesselImp(ZPA\_L)$
end procedure

The above algorithm is not optimal as it contains redundant evaluations of the impedance. For example, one will separately compute the impedance corresponding

to $\alpha\beta r$ and $\beta\alpha r$ even though these values are the same. A more efficient approach, described in [24], is to record previously computed values of the impedance to avoid repeating calculations.

3. Numerical implementation. Using the construction described in section 2, we compute the Laplace transform of the impedance corresponding to a given tree. To use this result as a boundary condition in a major vessel, we note that (2.9) implies

$$P(t) = \int_0^t Z(\tau)Q(t-\tau)\,d\tau, \tag{3.1}$$

where all quantities are evaluated at the end of the outflow vessel[1] and $Z = \mathcal{L}^{-1}(\hat{Z})$.

To evaluate (3.1), we use a convolution quadrature approach (CQA) [19] which utilizes the values of the Laplace transform $\hat{Z} = \mathcal{L}(Z)$ rather than the values of Z. This allows us to avoid entirely the delicate numerical inversion of the Laplace transform [25] to go from $\hat{Z}$, computed in section 2, to Z, which we cannot access directly. Furthermore, convolution quadrature methods are provably convergent even in the case when the inverse Laplace transform of $\hat{Z}$ only exists in a weak sense [21].

3.1. Convolution quadratures. For the sake of completeness, the CQA is summarized below in the present context. Applying Mellin's inversion formula, we obtain

$$Z(\tau) = \frac{1}{2\pi i}\int_{\nu-i\infty}^{\nu+i\infty} \hat{Z}(\lambda)e^{\lambda\tau}\,d\lambda, \tag{3.2}$$

where the integration is taken along the vertical line $Re(\lambda) = \nu$ with ν being greater than the real part of all singularities of $\hat{Z}$. An analysis of the locations of the singularities of $\hat{Z}$ is provided in section 4. The CQA [19] consists of substituting (3.2) into (3.1),

$$P(t) = \frac{1}{2\pi i}\int_{\nu-i\infty}^{\nu+i\infty} \hat{Z}(\lambda)\,y(\lambda;t)\,d\lambda, \qquad y(\lambda;t) = \int_0^t e^{\lambda t}Q(t-\tau)\,d\tau \tag{3.3}$$

and observing that y is the unique solution to the initial value problem

$$y' = \lambda y + Q, \qquad y(0) = 0. \tag{3.4}$$

The next step in the CQA is to apply a multistep method to (3.4) and to approximate $P(n\Delta t)$ by replacing y the integral (3.3) with

$$\sum_{j=0}^{k} \alpha_j y_{n+j-k} = \Delta t \sum_{j=0}^{k} \beta_j(\lambda y_{n+j-k} + Q((n+j-k)\Delta t)), \tag{3.5}$$

where Δt is the time step size and the parameters α_j and β_j $(j = 0,\ldots,k)$ are the coefficients of the chosen multistep method. Even after approximating y by a multistep method, it is challenging to directly evaluate the improper integral in (3.3) numerically. The remaining analysis, also from [19], recasts this integral into a more computationally appealing form.

[1] The end of the outflow vessel is the beginning ($x = 0$) of the root vessel of the tree. From here on and for the sake of simplicity, we omit explicit mention of the spatial variables.

Consider the formal expansions

$$\mathbb{Y}(\zeta) = \sum_{n=0}^{\infty} y_n \zeta^n \quad \text{and} \quad \mathbb{Q}(\zeta) = \sum_{n=0}^{\infty} Q(n\Delta t)\zeta^n.$$

Multiplying (3.5) by ζ^n and summing yields

$$\mathbb{Y}(\zeta) = \left(\frac{\Xi(\zeta)}{\Delta t} - \lambda\right)^{-1} \mathbb{Q}(\zeta), \quad \text{where } \Xi(\zeta) = \frac{\alpha_0\zeta^n + \cdots + \alpha_k}{\beta_0\zeta^n + \cdots + \beta_k}. \tag{3.6}$$

Evaluating (3.3) at discrete times $n\Delta t$ ($n = 0, 1, \dots$), we consider an expansion of P similar to (3.6),

$$\begin{aligned}\sum_{n=0}^{\infty} P_n\zeta^n &= \frac{1}{2\pi i}\int_{\nu-i\infty}^{\nu+i\infty} \hat{Z}(\lambda)\mathbb{Y}(\zeta)\,d\lambda \\ &= \frac{1}{2\pi i}\int_{\nu-i\infty}^{\nu+i\infty} \hat{Z}(\lambda)\left(\frac{\Xi(\zeta)}{\Delta t} - \lambda\right)^{-1} \mathbb{Q}(\zeta)\,d\lambda,\end{aligned}$$

where P_n is the approximation of (3.3) obtained by approximating y by (3.5). Cauchy's integral formula leads to

$$\sum_{n=0}^{\infty} P_n\zeta^n = \hat{Z}\left(\frac{\Xi(\zeta)}{\Delta t}\right)\mathbb{Q}(\zeta). \tag{3.7}$$

We then expand $\hat{Z}$ as

$$\hat{Z}\left(\frac{\Xi(\zeta)}{\Delta t}\right) = \sum_{n=0}^{\infty} z_n\zeta^n, \qquad z_n = \frac{1}{2\pi i}\int_{|\zeta|=r} \hat{Z}\left(\frac{\Xi(\zeta)}{\Delta t}\right)\zeta^{-n-1}\,d\zeta, \tag{3.8}$$

so that (3.7) becomes

$$\sum_{n=0}^{\infty} P_n\zeta^n = \sum_{n=0}^{\infty} z_n\zeta^n \sum_{n=0}^{\infty} Q(n\Delta t)\zeta^n.$$

Equating the like powers of ζ, we approximate the pressure P by

$$P(n\Delta t) \approx P_n = \sum_{j=0}^{n} z_{n-j}Q(j\Delta t). \tag{3.9}$$

During a simulation, (3.9) is enforced at the end of each outflow vessel.

It remains to compute the weights z_n, $n = 0, \dots, N$, where N is the total number of time steps. Following [20], this can be efficiently done through a trapezoidal rule approximation of the Cauchy integral in (3.8). More precisely, we approximate z_n by

$$\tilde{z}_n = \frac{r^{-n}}{M}\sum_{m=0}^{M-1} \hat{Z}\left(\frac{\Xi(r\,e^{im2\pi/M})}{\Delta t}\right)e^{-inm2\pi/M}, \tag{3.10}$$

where M is the number of quadrature points. The $\tilde{z}_n$'s can be computed simultaneously using FFT; this requires M evaluations of $\hat{Z}$ and $\mathcal{O}(M\log M)$ arithmetical operations. If $\hat{Z}$ is computed with an accuracy of $O(\epsilon)$, one may compute z_n, $n = 0, \dots, N$ with accuracy $O(\sqrt{\epsilon})$ by choosing $M = N$ and $r^N = \sqrt{\epsilon}$ [20]. For safety, we typically take $M = 2N$. We set $\epsilon = 10^{-10}$, but nearly identical results were obtained for ϵ ranging from 10^{-6} to 10^{-13}. In our numerical simulations, we use $\Xi(\zeta) = \zeta^2/2 - 2\zeta + 3/2$, which corresponds to the second order backward differentiation formula.

3.2. Impedance implementation algorithm. The algorithm for computing the impedance weights z_n with the CQA is as follows.

procedure ImpedanceWeights
Input:
t_f = final simulation time,
Δt = time step size,
N = number of time steps ($N = t_f/\Delta t$),
ϵ = accuracy of computation of $\hat{Z}$
Output:
impedance weights z_n, $n = 0, \ldots, N$
$M = 2N$,
$r = \epsilon^{1/2N}$
for $m = 0 : M - 1$ **do**
$\zeta = re^{i2\pi m/M}$,
$\Xi = \frac{1}{2}\zeta^2 - 2\zeta + \frac{3}{2}$,
$Z^{(m)} = \hat{Z}\,(\Xi/\Delta t)$
end for
for $n = 0 : N$ **do**
$z_n = \frac{r^{-n}}{M} \sum_{m=0}^{M-1} Z^{(m)} e^{-i2\pi mn/M}$
end for
end procedure

We compute the impedance weights for each outflow vessel prior to running a simulation; this requires $2N$ evaluations of $\hat{Z}$ per outflow vessel. The periodic structured tree condition requires N_T evaluations of the impedance, where N_T is the number of time steps per period. In most practical cases, N is a small multiple of N_T and the costs of both conditions are comparable.

The evaluation of $\hat{Z}$ is done directly and requires a few thousand floating point operations for the vascular trees considered here. One evaluation corresponds to $\mathcal{O}(\ell^2)$ floating point operations, where ℓ is the number of generations in the structured tree. Typically, ℓ is no more than 30. Both boundary conditions can thus be implemented at very low cost. Impedance boundary conditions on networks with many outlets and/or long time integration may require access to a large number of computed values.

4. Singularities of the Laplace transform of impedance. The location of the singularities of the Laplace transform of the impedance plays a critical role in the implementation of the general structured tree boundary condition. For instance, the CQA requires the existence of a real number ν such that for any singularity s^*, $\Re s^* \leq \nu$. Additionally, locations of the singularities of $\hat{Z}(s)$ play a critical role in section 5, where we compare the general condition to the original, periodic version. Unfortunately, characterizing the singularities of $\hat{Z}(s)$ is not trivial since the impedance is only defined algorithmically as a repeated composition of (2.10) and (2.11). However, by analyzing the properties of the maps (2.10) and (2.11) individually, we prove that the impedance has only one singularity with nonnegative real part: a removable singularity at $s = 0$.

Theorem 4.1. *If the terminal impedance $\hat{Z}_{term}$ has nonnegative real part, i.e., $\Re\hat{Z}_{term} \geq 0$, then the Laplace transform of the impedance of the structured tree, as defined in section* 2*, has no singularities for any s such that $\Re s \geq 0$, $s \neq 0$. There is a removable singularity at $s = 0$.*

Proof. The Laplace transform of the impedance is a repeated composition of

the maps (2.10) and (2.11). Its possible singularities can be differentiated into seven different cases:

Singularities of (2.10)

1. $s = 0$.
2. $d_s = 0$ or $s = -\delta$.
3. For some vessel in the tree, $s(s + \delta)$ is not in the region of analyticity of the square root function.
4. L/d_s is a singularity of tanh.
5. $sd_sC \tanh(L/d_s)\hat{Z}(s, L) + 1 = 0$.

Singularities of (2.11)

6. $\hat{Z}(s, 0) = 0$.
7. For some junction in the tree, $\hat{Z}_{d1}(s, 0) = -\hat{Z}_{d2}(s, 0)$.

The proof consists of eliminating all the above cases (see Appendix A). ∎

5. Connection to periodic version of structured tree. We investigate how our general structured tree boundary condition compares with the original boundary condition, which assumes periodicity in time. In section 5.1, we show that for flow regimes that are periodic, both boundary conditions yield the same solution. Furthermore, we have found that even in nonperiodic regimes, the two boundary conditions give startlingly similar results. An explanation for this phenomenon is given in section 5.2.

5.1. Comparison for periodic flows. If P and Q are periodic with period T, then

$$\frac{\hat{P}(i\omega_k)}{\hat{Q}(i\omega_k)} = \frac{\int_0^T P(t)e^{-i\omega_k t}dt}{\int_0^T Q(t)e^{-i\omega_k t}dt} = \frac{\hat{P}_k}{\hat{Q}_k},$$

where $\hat{P}(i\omega_k)$ and $\hat{Q}(i\omega_k)$ denote the Laplace transforms of pressure and flowrate evaluated at $i\omega_k$ with $\omega_k = 2\pi k/T$, and $\hat{P}_k$ and $\hat{Q}_k$ are the respective Fourier coefficients of P and Q.

Furthermore, the Laplace transform of the impedance satisfies $\hat{Z}(i\omega_k) = \hat{Z}_k$, where $\hat{Z}_k$ denotes the kth Fourier coefficient of the impedance [9]. For periodic flow and pressure, enforcing $\hat{Z}(s) = \hat{P}(s)/\hat{Q}(s)$, as is done in the general structured tree condition derived in this paper, implies $\hat{Z}_k = \hat{P}_k/\hat{Q}_k$, meaning the *periodic* boundary condition is also satisfied. Thus, in a simulation with periodic inflow velocity data, one obtains the same solution from the periodic structured tree boundary condition and our general structured tree condition (neglecting the effects of discretization error).

5.2. Comparison for nonperiodic flows. Both the periodic and general structured tree conditions express the pressure as a dot product (discrete convolution) of flow-rate history with impedance weights z_ℓ,

$$P(n\Delta t) = \sum_{\ell=0}^{n} z_\ell Q((n - \ell)\Delta t). \tag{5.1}$$

For the general condition, the impedance weights are determined through the CQA applied to the Laplace transform of the impedance in (3.10). For the periodic condition, the weights are determined by an inverse discrete Fourier transform of values of $\hat{Z}_k \triangleq \hat{P}_k/Q_k$, where $\hat{Z}_k$ are computed in a manner analogous to $\hat{Z}(s)$ (see [9] for full

details). Explicitly, the impedance weights for the periodic condition are

$$z_\ell = \begin{cases} \dfrac{\Delta t}{T} \sum_{k=-(N_T-1)/2}^{(N_T-1)/2} \hat{Z}_k e^{i\omega_k \ell \Delta t} & \text{for } \ell < N_T, \\ 0 & \text{for } \ell \geq N_T, \end{cases} \tag{5.2}$$

where $\omega_k = 2\pi k/T$ with T being the assumed period of P and Q. N_T is the number of time steps per period, so $z_\ell = 0$ for $\ell \geq N_T$ as the periodic condition considers only flow-rate history over the previous period.

Although the derivation of the periodic structured tree condition requires the pressure and flowrate to be periodic in time, the resulting numerical implementation, (5.1), in no way forces the solution to be periodic. Therefore, it is *possible* to apply the periodic structured tree boundary condition to *any* type of flow even in the absence of any justification for doing so. We compare this approach to the general structured tree boundary condition developed in this paper. Figure 5.1 displays the weights generated by each condition for the left posterior cerebral artery in the Circle of Willis, a ring-like structure of arteries in the human brain. Details about the Circle of Willis and parameter values used to generate these weights are given in section 5.4.

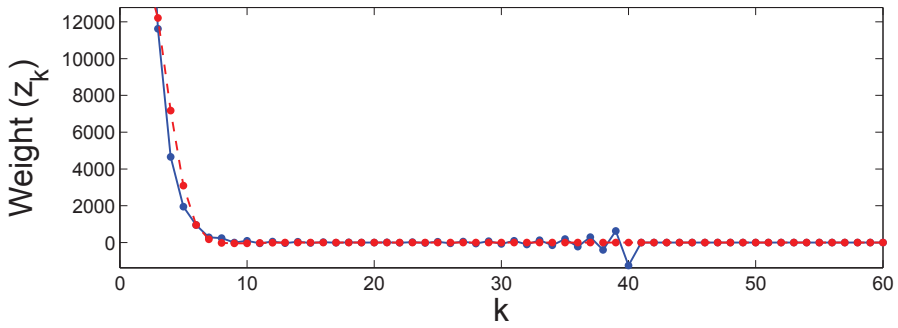

FIG. 5.1. *Comparison of the impedance weights generated by the periodic (blue (in the electronic version) solid curve) and general (red (in the electronic version) dashed curve) structured tree boundary conditions.*

The similarity of the weights for both methods suggests that solutions obtained by using either boundary condition may be similar, even for nonperiodic problems. This hypothesis is tested via numerical experiments in the Circle of Willis. We consider experiments with three different velocities applied to the inflowing vessels:

Experiment 1. Raw, quasi-periodic measured velocity data.

Experiment 2. The raw data in experiment 1 that have been averaged and made periodic with period 1 second.

Experiment 3. The periodic data from experiment 2 is used in all vessels except the left internal carotid artery, whose inflow velocity undergoes a rapid 50% decrease beginning at $t = 2$.

The velocity for each experiment is displayed in Figure 5.2. Section 5.4 contains additional technical details on these simulations, such as discretization scheme, parameter values, network description, and how the velocity data was obtained.

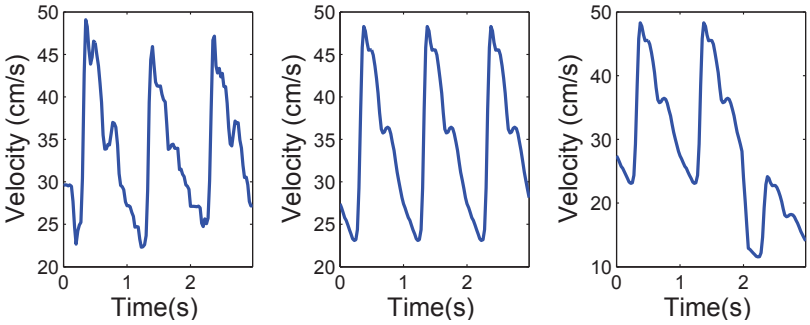

FIG. 5.2. *Inflow velocity curves for the left internal carotid for each of the three numerical experiments.*

For each simulation, we measure the difference between the periodic and general structured tree solutions by computing the L^2 norm of the difference between the two solutions at each spatial point for both state variables (A and Q). The solutions at the spatial point in the Circle of Willis with the largest difference are displayed in Figure 5.3. As expected from the proximity of the weights, the solutions obtained by the two methods are remarkably similar.

The similarity between the periodic and general conditions is not coincidental. We now show that the numerical implementation of the periodic condition may be viewed as a rough approximation of the general condition $\hat{Z}(s) = \hat{P}(s)/\hat{Q}(s)$. Crucial to this argument is the central result of section 4, which states that $\hat{Z}(s)$ has only one singularity for $\Re s \geq 0$: a removable singularity at $s = 0$.

If Q is twice differentiable and $Q(0) = Q'(0) = 0$, then $\hat{Z}(s) = \hat{P}(s)/\hat{Q}(s)$ is equivalent to

$$P(t) = \int_0^t \mathcal{L}^{-1}\left[\frac{\hat{Z}(s) - \hat{Z}_R}{s^2}\right](t-\tau)Q''(\tau)d\tau + \hat{Z}_R Q(t). \tag{5.3}$$

In (5.3), $\hat{Z}_R = \lim_{s\to\infty} \hat{Z}(s) = \sqrt{\rho/(A_0 C)}$, by (2.10). It is possible to show that $\hat{Z}(s)$ is bounded for $\Re s \geq 0$, and therefore, the inverse Laplace transform of $\hat{Z}(s)/s^2$ exists and is continuous (see [39, Lemma 3.6-1]). By approximating the integral corresponding to the inverse Laplace transform by a rectangle rule, we can rewrite (5.3) as

$$P(t) \approx \sum_{k=0}^{N_T-1} z_k Q((N_T - k)\Delta t), \tag{5.4}$$

where z_k denotes the impedance weights in (5.2) computed by the inverse discrete Fourier transform. Appendix B includes details of the derivation of (5.4), which implies that the *periodic* boundary condition corresponds to a numerical approximation of the *general* boundary condition.

5.3. Numerical issues with the periodic condition. The impedance weights for the periodic condition, although fairly close to the weights for the general condition, are oscillatory (Figure 5.1). Additionally, even in a simulation with periodic

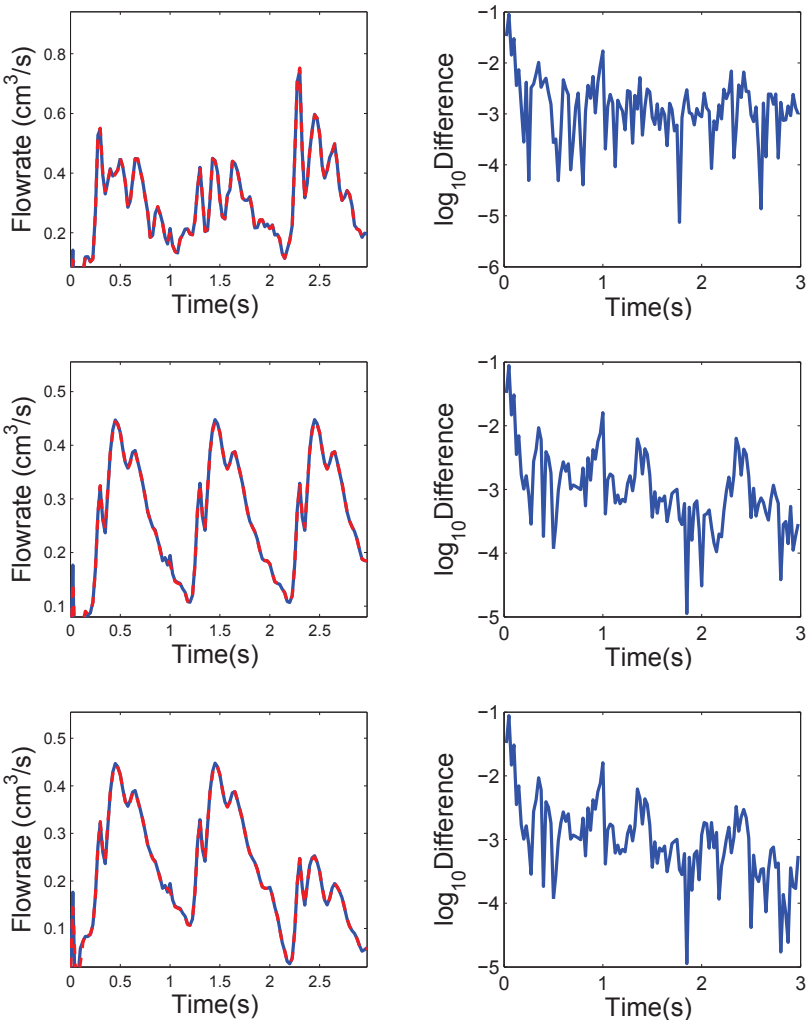

FIG. 5.3. *Top row: Left: solutions for a simulation using raw inflow velocity data with the periodic (blue (in the electronic version) solid curve) and general (red (in the electronic version) dashed curve) structured tree boundary conditions (experiment* 1*). The solution is plotted at a node in the Right Posterior Communicating Artery, which displays the largest difference in the network. Right: logarithm of the absolute value of the difference between the two methods at that point. Middle row: idem for periodic inflow velocity data (experiment* 2*). Bottom row: idem for periodic inflow velocity data that experiences a rapid decrease at* $t = 2$ *with the periodic (experiment* 3*).*

inflow velocity, the periodic structured tree condition exhibits oscillations near $t = 1$ (middle of Figure 5.3).

Another issue is that even in a simulation with periodic inflow velocity, the solution using the periodic condition converges to a periodic regime at a *slower* rate than the solution obtained from the general condition. To quantify this, we rewrite the solution "modulo T" into a sequence of grid functions

$$\mathcal{A}_k(x, t_n) = A(x, t_n + kT) \quad \text{and} \quad \mathcal{Q}_k(x, t_n) = Q(x, t_n + kT).$$

We also define quantities which measure the relative change in the solution from one period to the next,

$$\Delta_k \mathcal{A} \triangleq \max_{\substack{n=1,\dots,N_T \\ x\in\Omega}} \left| \frac{\mathcal{A}_{k+1}(x,t_n) - \mathcal{A}_k(x,t_n)}{\frac{1}{N_T}\sum_{n=1}^{N_T} \mathcal{A}_{k=1}(x,t)} \right|,$$

and similarly for $\mathcal{Q}_k$, where Ω is the set of all spatial points in the network. Figure 5.4 displays values of $\Delta_k = \max\{\Delta_k \mathcal{A}, \Delta_k \mathcal{Q}\}$ for each boundary condition for the simulation of the Circle of Willis with periodic inflow velocity data (Figure 5.3, middle). Remarkably, the solution from the general condition converges to a periodic regime at a substantially faster rate than the solution obtained from the periodic condition.

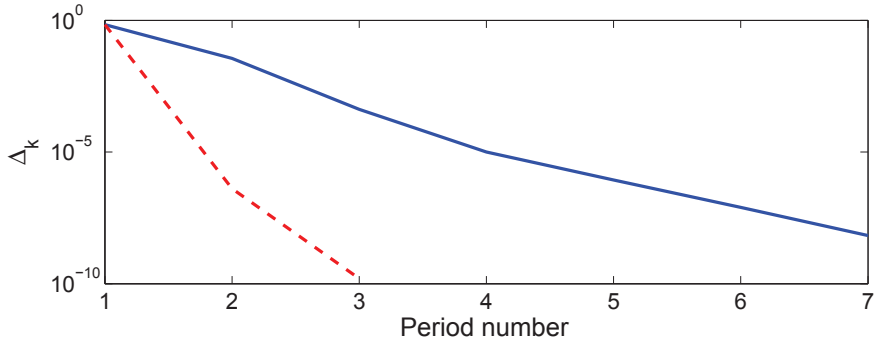

FIG. 5.4. *Values of Δ_k for the periodic (blue (in the electronic version) solid line) and general (red (in the electronic version) dashed line) structured tree conditions, showing that the general condition yields a solution converging to periodicity at a much faster rate than the original, periodic condition.*

We provide an analysis of this phenomenon for the linearized equations (2.5) and (2.6) in a network consisting of a single vessel. Rather than fixing the velocity at the inlet, we fix the flowrate. Discretizing the system using Chebyshev collocation in space combined with backward Euler time integration yields

$$\vec{P}^{n+1} = \vec{P}^n - \frac{\Delta t}{C} D\vec{Q}^{n+1}, \tag{5.5}$$

$$\vec{Q}^{n+1} = \vec{Q}^n - \Delta t \left[\frac{A_0}{\rho} D\vec{P}^{n+1} + \delta \vec{Q}^{n+1} \right], \tag{5.6}$$

where D denotes the Chebyshev differentiation matrix, and $\vec{P}^n = [P_0^n, \dots, P_M^n]^T$ is the vector of pressure values at time $n\Delta t$, i.e., $P_k^n \approx P(x_k, n\Delta t)$, where x_k is the kth of the $M+1$ Chebyshev nodes. To account for the inlet boundary condition, we replace the first equation in (5.6) by $Q_0^{n+1} = q_{n+1}$, where q is the imposed flowrate that is periodic ($q_n = q_{n+N_T}$ for all n). To account for the structured tree condition, we replace equation $M+1$ of (5.5) by

$$P_M^{n+1} = \sum_{k=0}^{N_T-1} z_k Q_M^{n+1-k}.$$

We express the map from period k onto period $k+1$ as

$$R\begin{bmatrix} \vec{P}^{(k+1)N_T} \\ \vec{Q}^{(k+1)N_T} \\ \vec{P}^{(k+1)N_T+1} \\ \vec{Q}^{(k+1)N_T+1} \\ \vdots \\ \vec{P}^{(k+2)N_T-1} \\ \vec{Q}^{(k+2)N_T-1} \end{bmatrix} = S\begin{bmatrix} \vec{P}^{kN_T} \\ \vec{Q}^{kN_T} \\ \vec{P}^{kN_T+1} \\ \vec{Q}^{kN_T+1} \\ \vdots \\ \vec{P}^{(k+1)N_T-1} \\ \vec{Q}^{(k+1)N_T-1} \end{bmatrix} + \begin{bmatrix} \vec{q}^{\,0} \\ \vec{q}^{\,1} \\ \vdots \\ \vec{q}^{\,N_T-1} \end{bmatrix}, \tag{5.7}$$

where the $(M+2)$nd component of the vector $\vec{q}^{\,n+1}$ equals q_{n+1} and all other components of $\vec{q}^{\,n+1}$ are 0, and the matrices R and S are block Toeplitz. The vector of flowrates does not depend on k due to the periodicity of the flowrate imposed at the inlet. We regard the mapping from one period to the next as a fixed point iteration and quantify the rate of convergence by analyzing the spectral radius of $R^{-1}S$ for the periodic and general structured tree conditions. The inverse of R was computed semi-analytically and the spectral radius was computed using MATLAB's eig command. This was done for each of the outflowing vessels of the Circle of Willis (Figure 5.5). The results, displayed in Table 5.1, show that the spectral radius corresponding to the general condition is many orders of magnitude smaller than the spectral radius corresponding to the periodic condition. This is in agreement with the behavior observed in Figure 5.4, where the solution obtained from the periodic structured tree converged to a periodic regime substantially slower than the solution obtained from the general structured tree condition.

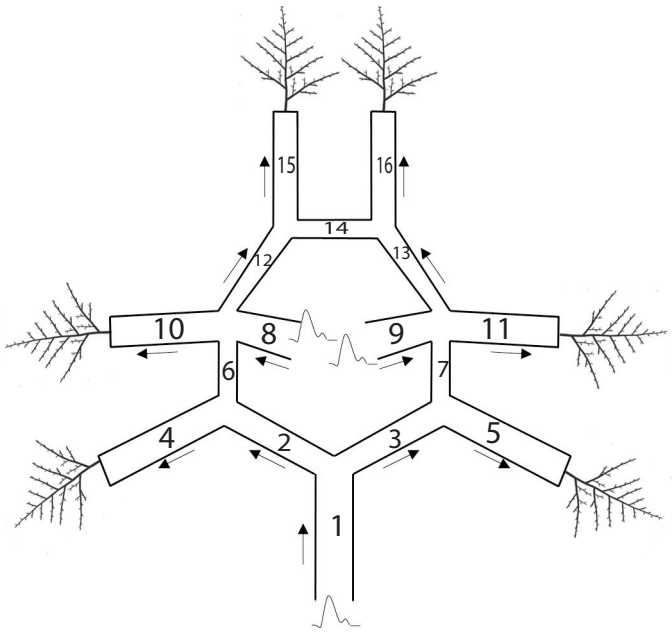

FIG. 5.5. *Schematic of the Circle of Willis. The curves at the inflow vessels correspond to the use of measured velocity data as a boundary condition, and the tree-like structures attached to the outflow vessels indicate the use of the structured tree as a boundary condition.*

TABLE 5.1
Spectral radii of $R^{-1}S$ in (5.7) for the periodic and general structured tree conditions.

Vessel	R PCA	L PCA	R MCA	L MCA	R ACA	L ACA
Periodic spectral radius	3.7e-03	3.3e-03	5.8e-03	5.2e-03	1.4e-02	8.0e-03
General spectral radius	4.5e-15	4.5e-14	1.2e-12	6.0e-12	1.4e-16	2.5e-13

TABLE 5.2
Names and measured length/radii data (in cm) for the Circle of Willis (Figure 5.5). Data are from [10]. r_{min} values are optimized values from [9]. BA = Basilar Artery, PCA = Posterior Cerebral Artery, PCoA = Posterior Communicating Artery, ICA = Internal Carotid Artery, MCA = Middle Cerebral Artery, ACA = Anterior Cerebral Artery, AcoA = Anterior Communicating Artery.

	Name	r_0	L	r_{min}
1	BA	0.15	0.825	N/A
2	R. PCA 1	0.112	0.333	N/A
3	L. PCA 1	0.112	0.333	N/A
4	R. PCA 2	0.110	0.756	0.0109
5	L. PCA 2	0.110	0.756	0.0083
6	R. PCoA	0.0986	1.00	N/A
7	L. PCoA	0.0986	1.00	N/A
8	R. ICA	0.210	4.81	N/A
9	L. ICA	0.210	4.81	N/A
10	R. MCA	0.134	2.11	0.0109
11	L. MCA	0.134	2.11	0.0095
12	R. ACA 1	0.170	1.07	N/A
13	L. ACA 1	0.100	1.07	N/A
14	ACoA	0.100	0.20	N/A
15	R. ACA 2	0.115	2.30	0.0198
16	L. ACA 2	0.115	2.30	0.0090

The slow convergence rate accompanying the periodic condition can have serious computational consequences. For example, the authors of [13] report that the periodic structured tree condition requires eight periods to converge to a periodic regime in their three-dimensional simulation of the cranial arterial tree, with one period requiring three hours of computation time. The results from this section indicate that the use of the general structured tree condition over the original, periodic version may yield substantial computational savings, even when one is performing simulations of blood flow that are periodic in time.

5.4. Numerical simulation details. To investigate various properties of our general structured tree boundary condition, we have implemented it in various numerical simulations of blood flow in the Circle of Willis (Figure 5.5 and Table 5.2). The actual results are interspersed in section 5. Here we give additional information pertaining to these numerical experiments.

Within each vessel of the Circle of Willis, we use (2.2) and (2.3) to model the hemodynamics. Proceeding as [12, 29], a characteristic study shows that, at standard operating regimes, changes in cross-sectional area and flowrate propagate at speed $U \pm S$, where $U = Q/A$ is the flow velocity and $S \gg |U|$. In other words, within each vessel, one scalar boundary condition is required at each end. There are three types of boundaries in this network: inflow/outflow boundaries and junctions. For inflow boundaries, we enforce $\frac{Q}{A} = U$, where U is velocity data measured using digital transcranial Doppler technology at the Beth Israel Deaconess Medical Center. For

outflow boundaries, we use the general structured tree boundary condition described in section 2, as well as the periodic structured tree condition described in [9] for comparison. At junctions, we impose conservation of mass and continuity of pressure; see [2, 10] for justification. Specifically, if at a particular junction there are m incoming vessels and n outgoing vessels, we enforce

$$\sum_{k=1}^{m} Q_{\mathrm{IN}}^{(k)}(t, L_k) = \sum_{k=1}^{n} Q_{\mathrm{OUT}}^{(k)}(t, 0),$$
$$P_{\mathrm{IN}}^{(1)}(t, L_1) = \cdots = P_{\mathrm{IN}}^{(m)}(t, L_m) = P_{\mathrm{OUT}}^{(1)}(t, 0) = \cdots = P_{\mathrm{OUT}}^{(n)}(t, 0),$$

where L_k denotes the length of vessel k.

To solve this boundary value problem, we use a Chebyshev collocation method with backward Euler time discretization. All numerical simulations were implemented with a time step size of 0.025 seconds and five spatial points per vessel. Grid refinement study indicates that these values are sufficient to ensure a relative accuracy of one percent. Parameter values used in these simulations are based on physiological data and can be found in Table 5.3 [23, 24].

TABLE 5.3
Parameters used for the numerical simulations in section 5.

Geometric parameters	$\alpha = 0.91$, $\beta = 0.58$, $\lambda = 50$
Fluid parameters	$\gamma = 2$, $\rho = 1.06\text{g cm}^{-3}$, $\mu = 0.0488\text{g cm}^{-1}\text{s}^{-1}$
Elastic relations	$C = 3\pi r^3/2Eh$, $Eh/r = k_1 e^{k_2 r} + k_3$
Elastic parameters	$k_1 = 2.00 \times 10^7\ \text{gs}^{-2}\text{cm}^{-1}$, $k_2 = -22.53\ \text{cm}^{-1}$ $k_3 = 8.65 \times 10^5\ \text{gs}^{-2}\text{cm}^{-1}$

6. Conclusions. Unlike most outflow boundary conditions in computational hemodynamics, structured tree boundary conditions [9, 22, 23, 24, 32] have the advantage of being physiologically based. However, their derivation is based on Fourier series arguments which only apply to strictly *periodic* flows—a significant restriction in practice.

The new general structured tree boundary condition proposed here is valid for *all* flows. The periodic conditions from [9, 22, 23, 24, 32] can be viewed as numerical approximations to the new one. Our analysis shows that the new and old conditions yield results which are remarkably similar. One of the practical implications of the present work is that the "traditional" structured tree boundary conditions may be used for nonperiodic flows even though they were not derived within that framework.

Cost and complexity being similar, the authors believe the new condition should be preferred over the old one both for periodic flows, as the numerical solution reaches periodicity much faster, and for general flows, as the new method has better stability properties.

Appendix A. Proof of Theorem 4.1. This appendix contains the auxiliary results (and corresponding proofs) necessary to the establishment of Theorem 4.1. The proof relies on eliminating the seven possible cases for the singularities of the impedance that are identified in section 4. Since the real part of expression (2.10) is unchanged under complex conjugation of s, we need only consider the quadrants $\Re s \geq 0$ and $\Im s \geq 0$. Additionally, we use the fact that $\delta, C, \rho, r_0, \mu, \nu$, and L are positive real constants due to their physiological meaning.

It is elementary to check that case 1 corresponds to a removable singularity. Since $\delta > 0$, case 2 is impossible. By Lemma A.1 below, case 3 cannot be realized. Lemma A.1 also implies that $\Re(L/d_s) > 0$; therefore case 4 is impossible since the singularities of tanh are purely imaginary.

Theorem A.7, which deals with the properties of (2.10) and relies on auxiliary Lemmas A.2–A.6, allows us to eliminate cases 5, 6, and 7. Since $\hat{Z}_{term}$ has nonnegative real part by assumption, it follows from Theorem A.7 that $\hat{Z}(s,0)$ has positive real part for any terminal vessel. Furthermore, for $\hat{Z}_{d1}(s,0)$ and $\hat{Z}_{d2}(s,0)$ with positive real part, the junction condition (2.11) implies that $\hat{Z}_{pa}(s,L)$ has positive real part as well. Therefore, in *any* vessel in the tree, $\hat{Z}(s,0)$ has positive real part and $\hat{Z}(s,L)$ has nonnegative real part, with $\Re[\hat{Z}(s,L)] = 0$ being possible only for terminal vessels. This fact, combined with Lemma A.5, implies that a singularity of case 5 is not possible. Also, since $\Re(\hat{Z}(s,0)) > 0$ for all vessels in the tree, singularities of cases 6 and 7 do not exist. This completes the proof of Theorem 4.1.

LEMMA A.1. *Let $s \in \mathbb{C}$ be nonzero in the first quadrant, i.e., $\Re s \geq 0$, $\Im s \geq 0$, and $s \neq 0$. Then $\Re\sqrt{s(s+\delta)} > 0$ and $\Im\sqrt{s(s+\delta)} \geq 0$, where δ is a positive real number. Moreover, $\Im\sqrt{s(s+\delta)} = 0$ only when $s \in \mathbb{R}$.*

Proof. The proof is elementary. ∎

LEMMA A.2. *Let $s \in \mathbb{C}$ such that $\Re s \geq 0$ and $\Im s \geq 0$. Then*

$$0 \leq \arg(sd_s) < \pi/4.$$

Proof. By definition of d_s in section (2),

$$\arg(sd_s) = \arg\sqrt{\frac{s}{s+\delta}} = \frac{1}{2}\left(\arg(s) - \arg(s+\delta)\right).$$

The desired inequalities follow from the fact that δ is real and positive. ∎

LEMMA A.3. *Let $z = x + iy \in \mathbb{C}$ such that $\Re z > 0$. Then*

$$\tanh(z) = \frac{\sinh(2x)}{\cosh(2x) + \cos(2y)} + i\frac{\sin(2y)}{\cosh(2x) + \cos(2y)}.$$

Proof. The proof is elementary. ∎

LEMMA A.4. *Let $z \in \mathbb{C}$ such that $\Re z > 0$ and $\Im z \geq 0$. Then*

$$\arg(\tanh(z)) \leq \arg(z),$$

with equality holding only when $\Im[z] = 0$.

Proof. The proof is elementary. ∎

LEMMA A.5. *Let $s \in \mathbb{C}$ such that $\Re s \geq 0$ and $\Im s \geq 0$. Then*

$$\Re[sd_s \tanh(L/d_s)] \geq 0,$$

with equality holding only when $s = 0$.

Proof. If $s \in \mathbb{R}$ and $s > 0$, then the result is obvious. We now show that if $\Im s > 0$, then $|\arg(sd_s \tanh(L/d_s))| < \pi/2$. By Lemmas A.1 and A.3, $\Re[\tanh(L/d_s)] > 0$, so $\arg[\tanh(L/d_s)] > -\pi/2$. Combining this with Lemma A.2 yields

$$\arg(sd_s \tanh(L/d_s)) = \arg(sd_s) + \arg(\tanh(L/d_s)) > -\pi/2.$$

For $\Im s > 0$, $\Im[\sqrt{s(s+\delta)}] > 0$ by Lemma A.1. Finally, according to Lemma A.4,

$$\arg(sd_s \tanh(L/d_s)) < \arg(s) + \arg(d_s) + \arg(1/d_s) = \arg(s) \leq \pi/2. \qquad \square$$

LEMMA A.6. *For any $s \in \mathbb{C}$ where $\Re[s] \geq 0, \Im[s] > 0$, the inequality*

$$\Im^2(a_s\overline{b_s}) < 4\Re(a_s)\Re(b_s)$$

is equivalent to

$$\cot\left[\arg\left(\tanh\left(\frac{L}{2d_s}\right)\right)\right] > \tan(\arg(sd_s)),$$

where a_s and b_s are defined in Theorem A.7.

Proof. The proof is omitted. Although lengthy, the proof is merely a straightforward application of numerous identities. $\square$

THEOREM A.7. *Consider the following family of mappings parameterized by s:*

$$F_s(z) = \frac{z + a_s}{b_s z + 1}, \qquad a_s = \frac{1}{sd_sC}\tanh\left(\frac{L}{d_s}\right), \qquad b_s = sd_sC\tanh\left(\frac{L}{d_s}\right).$$

For any $s \neq 0$ with nonnegative real part, F_s maps the region $\{z \in \mathbb{C}; \Re z \geq 0\}$ into the region $\{z \in \mathbb{C}; \Re z > 0\}$.

Proof. Consider the mapping F_s for a particular $s \neq 0$, where $\Re[s] \geq 0$ and $\Im[s] \geq 0$. We wish to show that $\Re[F_s(z)] > 0$ for any $z \in \mathbb{C}$, where $\Re[z] \geq 0$. Lemma A.5 implies b_s has positive real part and z has nonnegative real part by assumption, so the denominator of $F_s(z)$, $b_s z + 1$, is not zero. Therefore, $\Re[F_s(z)] > 0$ if and only if

$$\begin{aligned} 0 &< \Re\left[(z + a_s)\overline{(b_s z + 1)}\right], \\ &= \Re[b_s]\,|z|^2 + \Re[a_s\overline{b_s z}] + \Re\left[\overline{z}\right] + \Re[a_s]. \end{aligned}$$

Next, we write $z = x + iy$ and view the above function of a complex variable z as a function g_s of two real variables x and y. The above inequality is equivalent to the inequality

$$0 < \Re[b_s][x^2 + y^2] + \Re[a_s\overline{b_s}]x + \Im\left[a_s\overline{b_s}\right] y + x + \Re[a_s] \triangleq g_s(x, y)$$

holding for all $x \in [0, \infty]$ and $y \in \mathbb{R}$. We find the minimum of g_s by analyzing its partial derivatives,

$$\frac{\partial}{\partial x} g_s(x, y) = 2\Re\left[b_s\right] x + \Re\left[\frac{\overline{sd}}{sd}\right] |\tanh(L/d_s)|^2 + 1.$$

By Lemma A.5, $\Re[b_s] \geq 0$. Lemma (A.2) implies that $\Re[\overline{sd}/sd] \geq 0$, so g_s is increasing with respect to x. Therefore, the minimum of g_s in the right half plane occurs on the imaginary axis ($x = 0$) and this minimum is found as

$$\min_{x \geq 0, y \in \mathbb{R}} g_s(x, y) = \min_{y \in \mathbb{R}} g_s(0.y) = \Re(a_s) - \frac{\Im^2(a_s\overline{b_s})}{4\Re(b_s)}.$$

Therefore, Theorem A.7 is equivalent to the following inequality holding for all $s \neq 0$ with nonnegative real part:

$$\Im^2(a_s\overline{b_s}) < 4\Re(a_s)\Re(b_s).$$

If s is real, then a_s and b_s are real and positive so the above inequality holds trivially. If $\Im[s] > 0$, Lemma A.6 implies that the above inequality is equivalent to $\cot(\arg(\tanh(L/2d_s))) > \tan(\arg(sd_s))$. This inequality holds due to Lemma A.4 and the fact that $\arg s \geq \pi/2$. Indeed,

$$\cot(\arg(\tanh(L/2d_s))) > \cot(\arg(1/d_s)) = \tan(\pi/2 - \arg(1/d_s)) \geq \tan(\arg(sd_s)).$$

This completes the proof of Theorem A.7. ∎

Appendix B. Derivation of (5.4). For large enough values of t, $\mathcal{L}^{-1}[(\hat{Z}(s) - \hat{Z}_R)/s^2](t)$ becomes linear. This was observed through extensive numerical experiments, and can be shown analytically for a tree consisting of a single vessel. In implementing the periodic structured tree condition, one must prescribe a value of the expected period T (typically $T \approx 1$ second). In our numerical experiments, the convergence of $\mathcal{L}^{-1}[(\hat{Z}(s) - \hat{Z}_R)/s^2](t)$ to a linear regime occurs rather quickly, within 0.1 to 0.3 seconds. Therefore, for $t \geq T$, we approximate this inverse Laplace transform by a line $mt + b$. Replacing the inverse Laplace transform in (5.3) for $t \geq T$ with $mt + b$ yields

$$P(t) = I + I_2 + \hat{Z}_R Q(t), \qquad I = \int_{t-T}^{t} \mathcal{L}^{-1}\left[\frac{\hat{Z}(s) - \hat{Z}_R}{s^2}\right](t-\tau)Q''(\tau)d\tau$$

with

$$I_2 = \int_0^{t-T} (m(t-\tau) + b)\, Q''(\tau)d\tau = (mT + b)\, Q'(t-T) + m\, Q(t-T).$$

Since $\hat{Z}(s)/s^2 \sim \mathcal{O}(1/s^2)$, the integral corresponding to the inverse Laplace transform operator converges uniformly for $\tau \in [0, t]$. It is, therefore, valid to interchange the inverse Laplace operator with the outer integral. Integration by parts leads to

$$I = -Q'(t-T)\mathcal{L}^{-1}\left[\frac{\hat{Z}(s) - \hat{Z}_R}{s^2}\right](T) + \mathcal{L}^{-1}\left[\frac{\hat{Z}(s) - \hat{Z}_R}{s}\int_{t-T}^{t} Q'(\tau)e^{-s\tau}d\tau\right](t).$$

Using the approximate linearity of $\mathcal{L}^{-1}[(\hat{Z}(s) - \hat{Z}_R)/s^2](t)$ for large t and integrating by parts again, we have

$$I \approx -Q'(t-T)\,(mT + b) - mQ(t-T) + \mathcal{L}^{-1}\left[(\hat{Z}(s) - \hat{Z}_R)\int_{t-T}^{t} Q(\tau)e^{-s\tau}d\tau\right](t).$$

Approximating the integral corresponding to the inverse Laplace transform (see (3.2)) by a rectangle rule with mesh width $2\pi/T$ yields

$$\begin{aligned} I \approx\ & -Q'(t-T)\,(mT + b) - mQ(t-T) \\ & + \sum_{k=-\frac{N_T-1}{2}}^{\frac{N_T-1}{2}} (\hat{Z}(i\omega_k + \sigma) - \hat{Z}_R)e^{(i\omega_k+\sigma)t}\frac{1}{T}\int_{t-T}^{t} Q(\tau)e^{-(i\omega_k+\sigma)\tau}d\tau. \end{aligned}$$

Since $\hat{Z}(s)$ has no singularities for $\Re s > 0$ (see section 4), σ may be any positive real number. Furthermore, $\hat{Z}(s)$ being continuous for all s with $\Re s \geq 0$, we take the limit as $\sigma \to 0$ to obtain

$$I \approx -Q'(t-T)\,(mT+b) - mQ(t-T) + \sum_{k=-\frac{N_T-1}{2}}^{\frac{N_T-1}{2}} (\hat{Z}_k - \hat{Z}_R) e^{i\omega_k t} \frac{1}{T} \int_{t-T}^{t} Q(\tau) e^{-i\omega_k \tau} d\tau,$$

where we have used the fact that $\hat{Z}(i\omega_k) = \hat{Z}_k$. Approximating the Fourier integral of Q with a discrete Fourier transform of $Q(t-(N_T-1)\Delta t), \ldots, Q(t)$ yields

$$I \approx -Q'(t-T)\,[mT+b] - mQ(t-T) + \sum_{k=-\frac{N_T-1}{2}}^{\frac{N_T-1}{2}} \hat{Z}_k \tilde{Q}_k^{(N_T)} e^{i\omega_k t} - Z_R Q(t).$$

This yields the following approximation of the general boundary condition:

$$P(t) \approx I + I_2 + Z_R Q(t) = \sum_{k=-\frac{N_T+1}{2}}^{\frac{N_T+1}{2}} \hat{Z}_k \tilde{Q}_k^{(N_T)} e^{i\omega_k t}.$$

This leads to (5.4).

Acknowledgments. This work was initiated at the Statistical and Applied Mathematical Sciences Institute (SAMSI) as part its 2011-12 program on Uncertainty Quantification. The authors are indebted to Vera Novak for the use of the cerebral blood velocity data, as well as to Mette Olufsen and Tim David for helpful discussions.

REFERENCES

[1] J. Alastruey, A. W. Khir, K. S. Matthys, P. Segers, S. J. Sherwin, P. R. Verdonck, K. H. Parker, and J. Peiró, *Pulse wave propagation in a model human arterial network: Assessment of* 1*-d visco-elastic simulations against in vitro measurements*, J. Biomech., 44 (2011), pp. 2250–2258.

[2] J. Alastruey, K. H. Parker, J. Peiró, S. M. Byrd, and S. J. Sherwin, *Modeling the circle of willis to assess the effects of anatomical variations and occlusions on cerebral flows*, J. Biomech., 40 (2007), pp. 1794–1805.

[3] J. Alastruey, K. H. Parker, J. Peiró, and S. J. Sherwin, *Lumped parameter outflow models for* 1*-d blood flow simulations: Effect on pulse waves and parameter estimation*, Commun. Comput. Phys., 4 (2008), pp. 317–336.

[4] A. C. L. Barnard, W. A. Hunt, W. P. Timlake, and E. Valey, *Theory of fluid flow in compliant tubes*, Biophys. J., 6 (1966), pp. 717–724.

[5] D. Bessems, C. G. Giannopapa, M. C. M. Rutten, and F. N. van de Vosse, *Experimental validation of a time-domain-based wave propagation model of blood flow in viscoelastic vessels*, J. Biomech., 41 (2008), pp. 284–291.

[6] A. Bui, I. D. Šutalo, R. Manasseh, and K. Liffman, *Dynamics of pulsatile flow in fractal models of vascular branching networks*, Med. Biol. Eng. Comput., 47 (2009), pp. 763–772.

[7] S. Čanić and E. H. Kim, *Mathematical analysis of the quasilinear effects in a hyperbolic model blood flow through compliant axi-symmetric vessels*, Math. Methods Appl. Sci., 26 (2003), pp. 1161–1186.

[8] R. B. Clipp and B. N. Steele, *Impedance boundary conditions for the pulmonary vasculature including the effects of geometry, compliance, and respiration*, IEEE Trans. Biomed. Eng., 56 (2009), pp. 862–870.

[9] W. Cousins and P. A. Gremaud, *Boundary conditions for hemodynamics: The structured tree revisited*, J. Comput. Phys., 231 (2012), pp. 6086–6096.
[10] K. DeVault, P. A. Gremaud, V. Novak, M. S. Olufsen, G. Vernières, and P. Zhao, *Blood flow in the circle of willis: Modeling and calibration*, Multiscale Model. Simul., 7 (2008), pp. 888–909.
[11] M. A. Fernández, V. Milišić, and A. Quarteroni, *Analysis of a geometrical multiscale blood flow model based on the coupling of ODEs and hyperbolic PDEs*, Multiscale Model. Simul., 4 (2005), pp. 215–236.
[12] L. Formaggia, D. Lamponi, and A. Quarteroni, *One-dimensional models for blood flow in arteries*, J. Engrg. Math., 47 (2003), pp. 251–276.
[13] L. Grinberg, T. Anor, E. Cheever, J. R. Madsen, and G. E. Karniadakis, *Simulation of the human intracranial arterial tree*, Philos. Trans. R. Soc. Lond. Ser. A Math. Phys. Eng. Sci., 367 (2009), pp. 2371–2386.
[14] L. Grinberg and G. E. Karniadakis, *Outflow boundary conditions for arterial networks with multiple outlets*, Annals Bio. Eng., 36 (2008), pp. 1496–1514.
[15] H. J. Kim, I. E. Vignon-Clementel, J. S. Coogan, C. A. Figueroa, K. E. Jansen, and C. A. Taylor, *Patient-specific modeling of blood flow and pressure in human coronary arteries*, Annals Bio. Eng., 38 (2010), pp. 3195–3209.
[16] T. Kind, T. J. C. Faes, J.-W. Lankhaar, A. Vonk-Noordegraaf, and M. Verhaegen, *Estimation of three- and four-element windkessel parameters using subspace model identification*, IEEE Trans. Biomed. Eng., 57 (2010), pp. 1531–1538.
[17] E. O. Kung, A. S. Lee, F. Medina, R. B. Wicker, M. V. McConnell, and C. A. Taylor, *In vitro validation of finite-element model of aaa hemodynamics incorporating realistic outlet boundary conditions*, J. Biomech. Eng., 133 (2011), 041003.
[18] D. Liu, N. B. Wood, N. Witt, A. D. Hughes, S. A. Thom, and X. Y. Xu, *Computational analysis of oxygen transport in the retinal arterial network*, Current Eye Res., 34 (2009), pp. 945–956.
[19] C. Lubich, *Convolution quadrature and discretized operational calculus.* I, Numer. Math., 52 (1988), pp. 129–145.
[20] C. Lubich, *Convolution quadrature and discretized operational calculus.* II, Numer. Math., 52 (1988), pp. 413–425.
[21] Ch. Lubich, *On the multistep time discretization of linear initial-boundary value problems and their boundary integral equations*, Numer. Math., 67 (1994), pp. 365–389.
[22] M. S. Olufsen, *Modeling the arterial system with reference to an anesthesia simulator*, Ph.D. thesis, Roskilde University, Roskilde, Denmark, 1998, pp. 95–120.
[23] M. S. Olufsen, *Structured tree outflow condition for blood in the larger systemic arteries*, Am. J. Physiol., 276 (1999), pp. H257–H268.
[24] M. S. Olufsen, C. S. Peskin, W. Y. Kim, E. M. Pederson, A. Nadim, and J. Larsen, *Numerical simulation and experimental validation of blood flow in arteries with structured-tree outflow conditions*, Annals Bio. Eng., 28 (2000), pp. 1281–1299.
[25] J. V. Moloney, P. O. Kano, and M. Brio, *Application of Weeks method for the numerical inversion of the Laplace transform to the matrix exponential*, Commun. Math. Sci., 3 (2005), pp. 335–372.
[26] A. Quarteroni, M. Tuveri, and A. Veneziani, *Computational vascular fluid dynamics: Problems, models and methods*, Comput. Vis. Sci., 2 (2000), pp. 163–197.
[27] P. Raymond, F. Merenda, F. Perren, D. Rüfenacht, and N. Stergiopulos, *Validation of a one-dimensional model of the systemic arterial tree*, Am. J. Physiol. Heart Circ. Physiol., 297 (2009), pp. H208–H222.
[28] S. J. Sherwin, V. Franke, J. Peiró, and K. Parker, *One-dimensional modelling of a vascular network in space-time variables*, J. Engrg. Math., 47 (2003), pp. 217–250.
[29] S. J. Sherwin, L. Formaggia, J. Peiró, and V. Franke, *Computational modeling of* 1*d blood flow with variable mechanical properties and its application to simulation of wave propagation in the human arterial system*, Internat. J. Numer. Methods Fluids, 43 (2003), pp. 673–700.
[30] R. L. Spilker, J. A. Feinstein, D. W. Parker, V. M. Reddy, and C. A. Taylor, *Morphometry-based impedance boundary conditions for patient-specific modeling of blood flow in pulmonary arteries*, Annals Bio. Eng., 35 (2007), pp. 546–559.
[31] B. N. Steele, M. S. Olufsen, and C. A. Taylor, *Fractal network model for simulating abdominal and lower extremity blood flow during resting and exercise conditions*, Comput. Meth. Biomech. Biomed. Eng., 10 (2007), pp. 39–51.
[32] B. N. Steele and C. A. Taylor, *Simulation of blood flow in the abdominal aorta at rest and during exercise using a* 1*-d finite element method with impedance boundary conditions*

derived from a fractal tree, in Proceedings of the 2003 ASME Summer Bioengineering Meeting, Key Biscayne, FL, 2003.

[33] M. G. Taylor, *Wave transmission through an assembly of randomly branching elastic tubes*, Biophys. J., 6 (1966), pp. 697–716.

[34] R. Torii, M. Oshima, T. Kobayashi, K. Takagi, and T. E. Tezduyar, *Coupling* 3*d fluid-structure interaction modeling of cerebral aneurysm with* 0*d arterial network model as boundary conditions*, Trans. Japan Soc. Simul. Tech., 1 (2009), pp. 81–90.

[35] I. E. Vignon-Clementel, C. A. Figueroa, K. E. Jansen, and C. A. Taylor, *Outflow boundary conditions for three-dimensional finite element modeling of blood flow and pressure in arteries*, Comput. Methods Appl. Mech. Engrg., 195 (2006), pp. 3776–796.

[36] I. E. Vignon-Clementel, C. A. Figueroa, K. E. Jansen, and C. A. Taylor, *Outflow boundary conditions for* 3*D simulations of non-periodic blood flow and pressure fields in deformable arteries*, Comput. Meth. Biomech., (2010), pp. 1–16.

[37] J. R. Womersley, *Oscillatory motion of a viscous liquid in a thin-walled elastic tube*, I: *The linear approximation for long waves*, Philos. Mag., 46 (1955), pp. 199–221.

[38] J. R. Womersley, *Oscillatory flow in arteries: The constrained elastic tube as a model of arterial flow and pulse transmission*, Phys. Med. Biol., 2 (1957), pp. 178–187.

[39] A. H. Zemanian, *Generalized Integral Transforms*, Interscience Publishers, New York, 1968.